Dual Discrete-Frequency Reconfigurable IPT System With High Misalignment Tolerance for Stable Power Transfer Over Extended Coupling Variation

Mingxing Xiong, Kai Song, *Senior Member, IEEE*, Fengshuo Yang, Yu Lan, Qingxuan Zhang,
Jinhai Jiang, *Member, IEEE*, and C. Q. Jiang, *Senior Member, IEEE*

***Abstract*—Maintaining stable power transfer remains a critical challenge in inductive power transfer (IPT) technology, with coil misalignment being a primary cause of power instability. To address this issue, this article proposes a dual discrete-frequency reconfigurable IPT system with high misalignment tolerance. By strategically switching operating frequencies, the compensation network dynamically reconfigures between a dual-coupled SP-S topology and a detuned S-S topology. Notably, the output power versus coupling coefficient (P–k) curves at both frequencies exhibit flat regions for stable power transfer. Through systematic parameter design, these flat regions are concatenated to achieve continuous stable power output over an extended coupling variation range. A 500-W prototype validates the proposed method, demonstrating merely 5% power fluctuation under 250% coupling variation ($k = 0.1$–0.25). This corresponds to ±320 mm lateral misalignment (80% of coil diameter) in the X-axis or 50 mm to 130 mm airgap variation (160% of nominal airgap) in the Z-axis. The system maintains high efficiency between 85.37% and 94.51% across the entire operating range.**

***Index Terms*—Coupling variation, frequency switching, inductive power transfer (IPT), reconfigurable topology, stable power transfer.**

I. Introduction

Inductive power transfer (IPT) technology, which utilizes alternating electromagnetic fields as the energy transmis-sion medium, enables contactless power transfer from power sources to loads. This technology has gained wide-spread adoption in diversified applications due to its inherent advantages in operational safety and system reliability [1]. Typical implementations include electric vehicles (EVs) [2], unmanned aerial vehicles [3], autonomous underwater vehicles [4], and implantable medical devices (IMDs) [5]. Nevertheless, coil misalignment inevitably occurs in most practical scenarios, leading to drastic fluctuations in coupling parameters between primary and secondary coils. These variations significantly degrade the output power stability of IPT systems [6]. Therefore, maintaining stable power transfer under wide coupling variations remains a critical challenge in advancing IPT technology.

To maintain stable power transfer, conventional approaches predominantly implement control strategies on either primary or secondary sides. For dc–dc converters [7], [8], the typical approach requires wireless communication to feedback detection signals to the primary side, where data transmission is vulnerable to electromagnetic interference. Moreover, the additional power converters introduce an additional power conversion stage, thereby increasing costs, form factor, and power losses. Regarding inverter-side control, three major modulation categories exist: pulse density modulation [9]; pulsewidth modulation [10]; and pulse frequency modulation (PFM) [11]. Although PFM provides the most straightforward and effective control approach, it may trigger frequency bifurcation in IPT systems under wide coupling variations, compromising system stability. Compensation network adaptation methods, such as variable inductors [12] or tunable capacitors [13], have been proposed for gain regulation. However, these solutions suffer from similar drawbacks including increased cost and excessive space requirements. While control-based solutions demonstrate effectiveness and precision in power stabilization, their performance becomes constrained under substantial coupling variations due to limited modulation headroom, leading to reduced efficiency, stability degradation, and escalated control complexity.

Magnetic coupler optimization and compensation topology design can achieve inherent coupling immunity and self regulating power output, significantly reducing control complexity. Current research on magnetic couplers primarily employs composite coil structures such as double-D pads [14], bipolar pads [15], tripolar pads [16], and solenoid pads [17]. These configurations improve misalignment tolerance through magnetic flux superposition or cancellation mechanisms, creating smoother flux density distributions to maintain relatively stable coupling levels under lateral displacement conditions [18]. An alternative approach involves hybrid topologies that combine two sub-systems with complementary output power versus coupling coefficient (P–k) characteristics. Through strategic cascade

Received 6 June 2025; revised 17 August 2025; accepted 20 September 2025. Date of publication 23 September 2025; date of current version 23 December 2025. This work was supported by the National Natural Science Foundation of China under Grant 52277006 and Grant 52377004. Recommended for publication by Associate Editor B. Lee. *(Corresponding author: Kai Song.)*

Mingxing Xiong, Kai Song, Fengshuo Yang, Yu Lan, Qingxuan Zhang, and Jinhai Jiang are with the School of Electrical Engineering and Automation, Harbin Institute of Technology, Harbin 150001, China (e-mail: mingxingxiong@stu.hit.edu.cn; kaisong@hit.edu.cn; fengshuoyang@stu.hit.edu.cn; yulan@stu.hit.edu.cn; 22s136195@stu.hit.edu.cn; jiangjinhai@hit.edu.cn).

C. Q. Jiang is with the Department of Electrical Engineering, City University of Hong Kong, Hong Kong (e-mail: chjiang@cityu.edu.hk).

Color versions of one or more figures in this article are available at https://doi.org/10.1109/TPEL.2025.3613702.

Digital Object Identifier 10.1109/TPEL.2025.3613702

connections and parametric optimization, such as series/parallel combinations of *LCC-LCC* and S-S topologies [19], [20] or interleaved *LCC*-S and S-*LCC* configurations [21], [22], stable power transfer can be main-tained within specific coupling ranges. However, improper cascade configurations may induce primary inverter over-current risks, while the mandatory use of specialized decoupl-ed magnetic couplers inevitably increases system complexity and cost. Compared with hybrid solutions, detuned topologies (e.g., S-S [23], *LCC*-S [24], and X-type [25]) offer simpler structures and lower implementation costs. Their intentional detuning generates non-monotonic *P*–*k* curves while facilitating zero-voltage switching (ZVS). Nevertheless, these topologies exhibit excessive power fluctuations exceeding 20% when facing 200%–250% coupling variations. Similarly, dual-coupled topologies like the *LCC*-S and *LCC-LCC* configurations reported in [26] and [27] demonstrate nonmonotonic *P*–*k* characteristics under specific resonant conditions. By magnetically coupling compensation inductors with transmission coils, these designs enhance power transfer under weak coupling conditions while providing intrinsic open/short-circuit protection. Practical limitations emerge when *X*-axis misalignment exceeds 150 mm (33.3%), causing output power to drop to approximately 56.8% of aligned-case performance, a level insufficient for most real-world applications.

While hybrid topologies present structural complexity and elevated costs in practical implementations, reliance on single-topology solutions (detuned or dual-coupled configurations) proves inadequate for real-world requirements. This dilemma has motivated the development of reconfigurable topologies that integrate two or more compensation networks exhibiting non-monotonic *P*–*k* curve segments. By dynamically switching between these topologies according to coupling variations, continuous stable power transfer can be achieved across extended coupling ranges. Conventional implementations [28], [29], [30], [31] utilize auxiliary switching components to reconfigure between detuned S-S and *LCC*-S topologies. This hardware switching mechanism inherently introduces abrupt impedance discontinuity at transition boundaries, where fundamentally non-complementary impedance characteristics between topologies induce critical power/efficiency transients during reconfiguration events. In contrast, frequency-switching strategies offer superior design flexibility and reduced hardware costs compared to physical topology switching. Unlike continuous frequency control [11] prone to frequency bifurcation phenomena under coupling variations, discrete frequency switching inherently avoids such instability. Historically applied to constant-current/constant-voltage charging under fixed coupling conditions [32], [33], frequency-switching mechanisms remain underexplored for stable power transfer across wide coupling variations. For instance, the dual-frequency S-S topology reported in [34] requires complex parameter design procedures lacking explicit analytical solutions, particularly for determining operational frequencies, which demand predefined frequency ranges and iterative computations. This empirical approach relying on designer experience lacks universality in engineering practice. Consequently, implementing frequency-induced topology reconfiguration to expand coupling ranges would provide enhanced design flexibility, enabling stable power transmission through a more component-efficient and straightforward methodology.

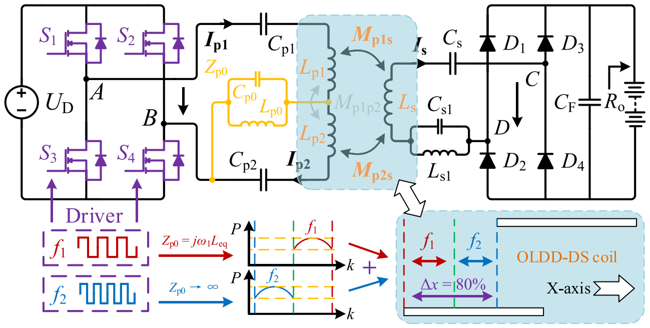

Fig. 1. Proposed reconfigurable IPT system with dual discrete-frequency.

This article proposes a dual discrete-frequency reconfigurable IPT system. Leveraging the open-circuit equivalence of parallel resonant loops at specific frequencies, the compensation network dynamically reconfigures between a dual-coupled SP-S topology and a detuned S-S topology through frequency switching. Both frequency-specific *P*–*k* curves exhibit distinct flat regions for stable power transfer. Through parametric optimization, these flat regions are concatenated at critical coupling coefficient, enabling continuous stable power transfer across an extended coupling variation range. Furthermore, a specially tailored magnetic coupler is developed to complement the proposed reconfiguration mechanism.

The rest of this article is organized as follows. Section II conducts comparative analysis of input-output characteristics between dual-coupled SP-S and detuned S-S topologies. Section III proposes a parametric design methodology and details the design of the magnetic coupler to extend the stable coupling range. Section IV validates the theoretical analysis through a 500-W prototype achieving 94.51% peak efficiency. Finally, Section V concludes this article.

II. THEORETICAL ANALYSIS

The proposed reconfigurable IPT system architecture is depicted in Fig. 1, comprising a dc voltage source (U_D) feeding a full-bridge inverter with power switches S_1-S_4, followed by a diode rectifier (D_1-D_4), output filter capacitor C_F, and battery load R_o. The magnetic structure incorporates dual primary coils with equal self-inductances ($L_{p1} = L_{p2} = L_p$) and a secondary coil with self-inductance L_s, carrying respective currents I_{p1}, I_{p2}, and I_s. The compensation network features primary-side components C_{p1}, C_{p2}, C_{p0}, and L_{p0} along with secondary-side elements C_s, C_{s1}, and L_{s1}, where Z_{p0} denotes the equivalent impedance of the C_{p0}-L_{p0} parallel branch. Mutual inductances are specifically constrained with $M_{p1s} = M_{p2s} = M_{ps}$ (identical magnitude and polarity) while maintaining $M_{p1p2} = 0$ to ensure decoupled primary coils. The physical realization of these precise electromagnetic conditions will be detailed in Section III, followed by their theoretical analysis.

The proposed IPT system operates at two discrete frequencies with distinct resonant conditions. When operating at f_1 ($\omega_1 = 2$

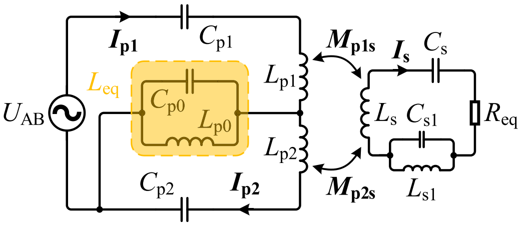

Fig. 2. Equivalent circuit of dual-coupled SP-S topology in f_1-mode.

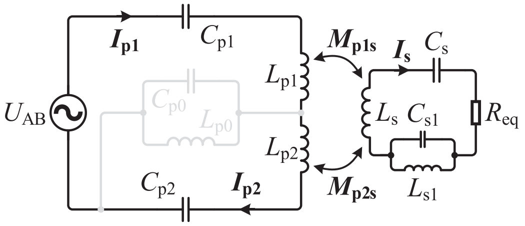

Fig. 3. Equivalent circuit of detuned S-S topology in f_2-mode.

πf_1), the system parameters satisfy:

$$\begin{cases} Z_{p0} = j\omega_1 L_{p0} / \left(1 - \omega_1^2 L_{p0} C_{p0}\right) = j\omega_1 L_{\text{eq}} \\ j\omega_1 L_p + 1/\left(j\omega_1 C_{p1}\right) + j\omega_1 L_{p0} / \left(1 - \omega_1^2 L_{p0} C_{p0}\right) = 0 \\ j\omega_1 L_p + 1/\left(j\omega_1 C_{p2}\right) + j\omega_1 L_{p0} / \left(1 - \omega_1^2 L_{p0} C_{p0}\right) = 0 \\ j\omega_1 L_s + 1/\left(j\omega_1 C_s\right) + j\omega_1 L_{s1} / \left(1 - \omega_1^2 L_{s1} C_{s1}\right) = 0 \end{cases} \tag{1}$$

where the C_{p0}-L_{p0} combination equivalently functions as an inductive component L_{eq}, effectively configuring the compensation network into a dual-coupled SP-S topology. Conversely, at f_2 ($\omega_2 = 2\pi f_2$) the system meets

$$\begin{cases} Z_{p0} \to \infty \Leftrightarrow 1 - \omega_2^2 L_{p0} C_{p0} = 0 \\ 2j\omega_2 L_p + 1/\left(j\omega_2 C_{p1}\right) + 1/\left(j\omega_2 C_{p2}\right) = 2j\alpha\omega_2 L_p \\ j\omega_2 L_s + 1/\left(j\omega_2 C_s\right) + j\omega_2 L_{s1} / \left(1 - \omega_2^2 L_{s1} C_{s1}\right) = 0 \end{cases} \tag{2}$$

where the detuning factor α is analytically defined to fulfill $0 < \alpha < 1$. Under this parameterization, the C_{p0}-L_{p0} pair enters parallel resonance (equivalent open-circuit), thereby morphing the compensation network into a detuned S-S topology. This frequency-dependent reconfiguration mechanism leverages the analytical relationships in (1) and (2) to dynamically alter the primary-side network topology while maintaining secondary-side series resonance. Consequently, the system achieves seamless transitions between dual-coupled SP-S and detuned S-S operational modes through discrete frequency switching without auxiliary switches, as subsequently analyzed.

A. f_1-Mode: Dual-Coupled SP-S Topology

When operating at f_1, the equivalent circuit is shown in Fig. 2, where U_{AB} denotes the inverter output voltage and R_{eq} represents the equivalent ac load preceding the rectifier

$$\begin{cases} U_{AB} = \frac{2\sqrt{2}}{\pi} U_D \\ R_{\text{eq}} = \frac{8}{\pi^2} R_o \end{cases}. \tag{3}$$

Applying Kirchhoff's voltage laws (KVL) to Fig. 2 yields the governing equations

$$\begin{cases} U_{AB} = \left(j\omega_1 L_p + 1/\left(j\omega_1 C_{p1}\right) + j\omega_1 L_{\text{eq}}\right) I_{p1} \\ -j\omega_1 L_{\text{eq}} I_{p2} - j\omega_1 M_{ps} I_s \\ 0 = \left(j\omega_1 L_p + 1/\left(j\omega_1 C_{p2}\right) + j\omega_1 L_{\text{eq}}\right) I_{p2} \\ -j\omega_1 L_{\text{eq}} I_{p1} - j\omega_1 M_{ps} I_s \\ 0 = \left(j\omega_1 L_s + 1/\left(j\omega_1 C_s\right) + j\omega_1 L_{s1} / \left(1 - \omega_1^2 L_{s1} C_{s1}\right)\right) I_s \\ -j\omega_1 M_{ps} I_{p1} - j\omega_1 M_{ps} I_{p2} \end{cases}. \tag{4}$$

Substituting (1) into (4) derives the coil currents

$$\begin{cases} I_{p1} = U_{AB} M_{ps}^2 / \left(L_{\text{eq}}^2 R_{\text{eq}} + 2j\omega_1 L_{\text{eq}} M_{ps}^2\right) \\ I_{p2} = U_{AB} \left(jL_{\text{eq}} R_{\text{eq}} + \omega_1 M_{ps}^2\right) / \left(\omega_1 L_{\text{eq}}^2 R_{\text{eq}} + 2j\omega_1^2 L_{\text{eq}} M_{ps}^2\right) \\ I_s = jU_{AB} M_{ps} / \left(2\omega_1 M_{ps}^2 - jL_{\text{eq}} R_{\text{eq}}\right) \end{cases}. \tag{5}$$

When the secondary coil exceeds permissible misalignment or disengages completely ($M_{ps} \to 0$), analysis confirms

$$\begin{cases} \lim\limits_{M_{ps} \to 0} I_{p1} = 0 \\ \lim\limits_{M_{ps} \to 0} I_{p2} = j\frac{U_{AB}}{\omega_1 L_{\text{eq}}} \end{cases}. \tag{6}$$

Equation (6) demonstrates bounded primary coil currents, preventing inverter overcurrent failures.

The input impedance Z_{in1} and its phase angle θ_{in1} at f_1 are derived as

$$\begin{cases} Z_{\text{in1}} = L_{\text{eq}}^2 R_{\text{eq}} / M_{ps}^2 + 2j\omega_1 L_{\text{eq}} \\ \theta_{\text{in1}} = \arctan\left[2\omega_1 M_{ps}^2 / \left(L_{\text{eq}} R_{\text{eq}}\right)\right] \end{cases}. \tag{7}$$

The inductive nature of Z_{in1} ($\theta_{\text{in1}} > 0$) inherently enables ZVS of inverter transistors.

Combining (1), (3), and (5), the output power P_{o1} versus coupling coefficient k_{ps} ($k_{ps} = M_{ps}/\sqrt{(L_p L_s)}$) is formulated

$$P_{o1}\left(k_{ps}\right) = \frac{1}{Ak_{ps}^2 + \frac{B}{k_{ps}^2}} \tag{8}$$

where $A = \pi^4 \omega_1^2 L_{\text{p}} L_{\text{s}} / (16 R_{\text{o}} U_{\text{D}}^2)$, $B = L_{\text{eq}}^2 R_{\text{o}} / (L_{\text{p}} L_{\text{s}} U_{\text{D}}^2)$.

Differentiating P_{o1} with respect to k_{ps} and setting $dP_{o1}/dk_{ps} = 0$ locates the extremum point (k_{ex1}, P_{o1_max})

$$\frac{\partial P_{o1}\left(k_{ps}\right)}{\partial k_{ps}} = 0 \Rightarrow k_{\text{ex1}} = \left(\frac{B}{A}\right)^{\frac{1}{4}} \Rightarrow P_{o1\_\text{max}} = \frac{1}{2\sqrt{AB}}. \tag{9}$$

The equivalent inductance L_{eq} is subsequently derived as

$$L_{\text{eq}} = \frac{\pi^2 \omega_1 L_p L_s k_{\text{ex1}}^2}{4R_o}. \tag{10}$$

As indicated in (8) and (9), P_{o1} exhibits a nonmonotonic relationship with k_{ps}, first increasing then decreasing beyond k_{ex1}. This creates a plateau region in the P_{o1}-k_{ps} curve, corresponding to a defined coupling variation interval that ensures stable power transfer.

B. f_2-mode: Detuned S-S Topology

When operating at f_2, the equivalent circuit in Fig. 3 yields the following governing equations through KVL:

$$\begin{cases} U_{AB} = \left(2j\omega_2 L_p + 1/\left(j\omega_2 C_{p1}\right) + 1/\left(j\omega_2 C_{p2}\right)\right) I_p \\ -2j\omega_2 M_{ps} I_s \\ 0 = \left(j\omega_2 L_s + 1/\left(j\omega_2 C_s\right) + j\omega_2 L_{s1}/\left(1-\omega_2^2 L_{s1} C_{s1}\right)\right) I_s \\ -2j\omega_2 M_{ps} I_p \end{cases}. \tag{11}$$

Substituting (2) into (11) resolves the current distribution

$$\begin{cases} I_p = U_{AB} R_{\mathrm{eq}}/\left(4\omega_2^2 M_{ps}^2 + 2j\omega_2 \alpha L_p R_{\mathrm{eq}}\right) \\ I_s = jU_{AB} M_{ps}/\left(2\omega_2 M_{ps}^2 + j\alpha L_p R_{\mathrm{eq}}\right) \end{cases} \tag{12}$$

where $I_{p1} = I_{p2} = I_p$.

Critical safety analysis under secondary coil disengagement ($M_{ps} \to 0$) reveals

$$\lim_{M_{ps}\to 0} I_p = \frac{U_{AB}}{2j\omega_2 \alpha L_p}. \tag{13}$$

Equation (13) confirms bounded primary currents, maintaining inherent overcurrent protection across operating modes.

The input impedance characteristics at f_2 are derived as

$$\begin{cases} Z_{\mathrm{in}2} = 4\omega_2^2 M_{ps}^2/R_{\mathrm{eq}} + 2j\alpha\omega_2 L_p \\ \theta_{\mathrm{in}2} = \arctan\left[\alpha L_p R_{\mathrm{eq}}/\left(2\omega_2 M_{ps}^2\right)\right] \end{cases}. \tag{14}$$

The persistently inductive $Z_{\mathrm{in}2}$ ($\theta_{\mathrm{in}2} > 0$) preserves ZVS capability across coupling variations.

Unifying (2), (3), and (12) establishes the f_2-mode output power relationship

$$P_{o2}\left(k_{ps}\right) = \frac{1}{Ck_{ps}^2 + \frac{D}{k_{ps}^2}} \tag{15}$$

where $C = \pi^4\omega_2^2 L_{\mathrm{p}} L_s/(2R_o U_{\mathrm{D}}^2$, $D = \alpha^2 L_{\mathrm{p}} R_o/(2L_s U_D^2)$.

Extrema analysis through $dP_{o2}/dk_{\mathrm{ps}} = 0$ locates

$$\frac{\partial P_{o2}\left(k_{ps}\right)}{\partial k_{ps}} = 0 \Rightarrow k_{\mathrm{ex}2} = \left(\frac{D}{C}\right)^{\frac{1}{4}} \Rightarrow P_{o2\_\max} = \frac{1}{2\sqrt{CD}}. \tag{16}$$

The detuning factor α is inversely resolved as

$$\alpha = \frac{\pi^2\omega_2 L_s k_{\mathrm{ex}2}^2}{4R_o}. \tag{17}$$

As demonstrated in (15) and (16), the P_{o2}-k_{ps} curve similarly exhibits a plateau region corresponding to stable power transfer within specific coupling ranges, complementing the f_1-mode characteristics through strategic parameter design to achieve continuous coverage across extended coupling variation.

III. SYSTEM DESIGN

A. Circuit Parameters Design

The power fluctuation coefficient δ is defined to quantify output stability:

$$\delta = \frac{P_{o\_\max} - P_{o\_\min}}{P_{o\_\max} + P_{o\_\min}} \times 100\% \tag{18}$$

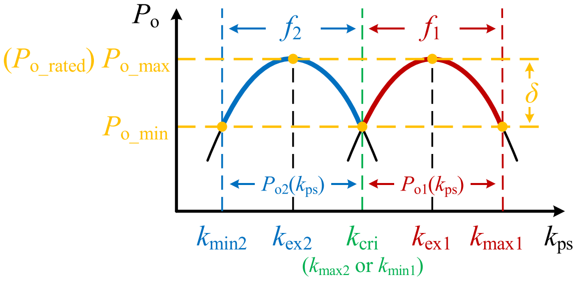

Fig. 4. Output power curve versus coupling.

where $P_{o\_\max}$ and $P_{o\_\min}$ represent the maximum/minimum allowable power levels, respectively, with P_{o_rated} preset at $P_{o\_\max}$ to prevent battery overvoltage/overcurrent.

Theoretical analysis in Section II reveals dual frequency-dependent power plateau regions corresponding to distinct coupling ranges [$k_{\min 1}$, $k_{\max 1}$] at f_1 (dual-coupled SP-S topology) and [$k_{\min 2}$, $k_{\max 2}$] at f_2 (detuned S-S topology). Continuous power transfer requires overlapping *P*–*k* curves at critical coupling coefficient k_{cri} ($k_{\max 2}$ or $k_{\min 1}$) with matched $P_{o\_\max}$, as illustrated in Fig. 4, yielding the constraint:

$$\begin{cases} P_{o2}\left(k_{\min 2}\right) = P_{o1}\left(k_{\max 1}\right) \\ P_{o2}\left(k_{\max 2}\right) = P_{o1}\left(k_{\min 1}\right) \\ P_{o2}\left(k_{\mathrm{ex}2}\right) = P_{o1}\left(k_{\mathrm{ex}1}\right) \end{cases}. \tag{19}$$

Substituting (8), (15), (18) into (19) establishes

$$\begin{cases} k_{\min 2} = \frac{2}{\pi\omega_2}\sqrt{\frac{\omega_1 L_{\mathrm{eq}} R_o}{\beta L_p L_s}} \\ k_{\mathrm{cri}} = \frac{2}{\pi}\sqrt{\frac{L_{\mathrm{eq}} R_o}{\omega_2 L_p L_s}} \\ k_{\max 1} = \frac{2}{\pi}\sqrt{\frac{\beta L_{\mathrm{eq}} R_o}{\omega_1 L_p L_s}} \end{cases} \tag{20}$$

where $\beta = (1+\sqrt{\delta})/(1-\sqrt{\delta})$.

Further combination of (8), (9), (15), (16), (18) with (19) reveals inherent coupling relationships:

$$k_{\min 2}^2 = \beta^{-1} k_{\mathrm{ex}2}^2 = \beta^{-2} k_{\mathrm{cri}}^2 = \beta^{-3} k_{\mathrm{ex}1}^2 = \beta^{-4} k_{\max 1}^2. \tag{21}$$

Simultaneous solution of (20) and (21) yields the frequency coordination equation

$$\frac{f_2}{f_1} = \beta = \frac{1+\sqrt{\delta}}{1-\sqrt{\delta}}. \tag{22}$$

Critically, (22) establishes a direct analytical relationship between f_1 and f_2, fundamentally distinct from method [34] that requires iterative computations within predefined frequency bounds. This explicit frequency-domain linkage enables customized f_1/f_2 combinations tailored to application-specific standard requirements, while eliminating the need for range-specific initialization or convergence iterations inherent in conventional frequency-sweeping approaches.

The input impedance characteristics are reformulated by substituting (10) and (17) into (7) and (14)

$$\begin{cases} Z_{\text{in}1} = \frac{\pi^2 \omega_1^2 L_p L_s k_{\text{ex}1}^2}{2R_o} \left(\frac{k_{\text{ex}1}^2}{k_{ps}^2} + j \right) \\ Z_{\text{in}2} = \frac{\pi^2 \omega_2^2 L_p L_s k_{\text{ex}2}^2}{2R_o} \left(\frac{k_{ps}^2}{k_{\text{ex}2}^2} + j \right) \\ \theta_{\text{in}1} = \arctan\left(\frac{k_{ps}^2}{k_{\text{ex}1}^2} \right) \\ \theta_{\text{in}2} = \arctan\left(\frac{k_{\text{ex}2}^2}{k_{ps}^2} \right) \end{cases}. \tag{23}$$

Equation (23) demonstrates anti-correlated variations of $Z_{\text{in}1}$-$Z_{\text{in}2}$ and $\theta_{\text{in}1}$-$\theta_{\text{in}2}$ with respect to coupling coefficient k_{ps}.

Furthermore, combining with (21), the phase angles are constrained within $\theta_{\text{in}} \in [\arctan(1/\beta), \arctan(\beta)]$.

Extracting the impedance constraints of the primary-side circuits from (1) and (2), and combining them with (10) and (17), yields the new parametric constraint:

$$\begin{cases} j\omega_1 L_p + \frac{1}{j\omega_1 C_{p1}} + j\frac{\pi^2 \omega_1^2 L_p L_s k_{\text{ex}1}^2}{4R_o} = 0 \\ 2j\omega_2 L_p + \frac{1}{j\omega_2 C_{p1}} + \frac{1}{j\omega_2 C_{p2}} = j\frac{\pi^2 \omega_2^2 L_p L_s k_{\text{ex}2}^2}{2R_o} \end{cases}. \tag{24}$$

Critically, (1) implies $C_{p1} = C_{p2}$, allowing substitution using either resonant loop equation.

Substituting (20), (21), and (22) into (24) solves for the key design parameter:

$$\begin{cases} C_{p1} = \frac{1}{\omega_1 \omega_2 L_p} \\ L_{\text{eq}} = (\beta - 1) L_p \end{cases}. \tag{25}$$

Back-substituting (25) into the remaining constraints of (1) and (2) determines the values of all other compensation components.

Equations (20)–(25) define the parametric framework enabling dual-frequency operation. While ensuring continuous power transfer through frequency coordination, the frequency mode boundaries remain governed by magnetic coupler characteristics, particularly coil parameters in (20) that determine both rated operation and switching thresholds. This coupling necessitates structural-parametric optimization of the coupler to align its spatial flux distribution with target coupling range, a process systematically addressed in the following subsection.

B. Magnetic Coupler Design

The proposed reconfigurable topology imposes specific electromagnetic constraints on the coupler design as derived from Section II analysis: primary coils L_{p1} and L_{p2} must maintain equal self-inductances, working mutual inductances M_{p1s} and M_{p2s} require identical magnitude and polarity, while cross mutual inductance M_{p1p2} should approach zero. These conditions translate to coupling coefficient requirements: working couplings $k_{p1s} = k_{p2s}$ (where $k_{pis} = M_{pis}/\sqrt{(L_{pi}L_s)}$, $i = 1, 2$) and cross coupling $k_{p1p2} = M_{p1p2}/\sqrt{(L_{p1}L_{p2})} < 0.05$ [15]. While overlapping DD (OLDD) coils with square secondaries theoretically meet these requirements, practical implementations exhibit limitations due to longitudinal flux concentration in square coils. As lateral misalignment increases, diminishing effective overlap area induces rapid k_{p1s} and k_{p2s} degradation. Peripheral flux-line bending generates unutilized transverse components in such configurations. In contrast, ferrite-enhanced solenoid coils exploit transverse flux through axis-symmetric magnetic steering [17]. This design maintains stable coupling by redirecting flux paths via high-permeability ferrite channels, significantly improving misalignment tolerance compared to OLDD-square configurations. The resultant expanded effective coupling range enables robust power transfer across practical positional variations.

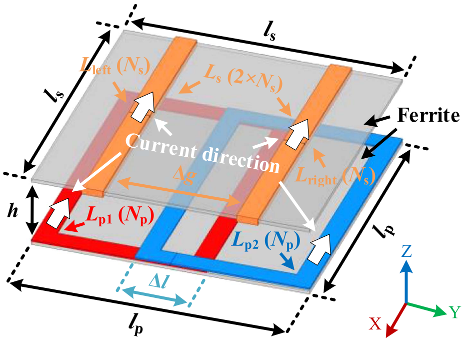

Fig. 5. Coil structure of the reconfigurable IPT system.

This article proposes a high misalignment tolerance magnetic coupler tailored for the reconfigurable topology, as depicted in Fig. 5. The primary side employs OLDD coils comprising two identical square coils (L_{p1} and L_{p2}) with reverse polarity, achieving decoupling through controlled overlap length Δl. The secondary utilizes a double-solenoid (DS) coil (L_s) wound on a ferrite core, where left (L_{left}) and right (L_{right}) sections, separated by a controlled gap Δg, are coaxially wound in-phase using Litz wire to satisfy k_{p1s} and k_{p2s} requirements. The DS coil architecture ensures $L_{\text{left}} = L_{\text{right}}$ in both geometry and turns, with mutual inductance $M_{\text{left-right}}$ between sections contributing to the total secondary inductance: $L_s = L_{\text{left}} + L_{\text{right}} + 2M_{\text{left-right}}$. Critical parameters are annotated in Fig. 5.

To enhance the misalignment tolerance of OLDD-DS coil within target coupling ranges, a systematic design procedure is proposed, as illustrated in Fig. 6. The framework incorporates four design parameters: primary/secondary coil turns (N_p, N_s) and geometric variables (Δl, Δg). Initial preset parameters include coil dimensions (l_p, l_s, h), wire diameters (d_p, d_s), power fluctuation δ, operating frequency f_1, load resistance R_o, and maximum coupling $k_{\max 1}$. Subsequent computations derive operating frequency f_2 and minimum coupling $k_{\min 2}$ through (20) and (22). Theoretical secondary self-inductance L_{s0} is precalculated via (25), enabling iterative optimization of secondary parameters (N_s, Δg). Primary parameters (N_p, Δl) are then refined under decoupling constraints and nominal coupling k_{ps0}. For each validated parameter set undergo X-axis misalignment characterization to determine the normalized maximum offset $\Delta x =$ (Maximum admissible offset at $k_{\min 2}$)$/l_p$, with the optimal set selected for maximum Δx.

A representative 400 × 400 mm design case, analytically constrained by (20) to ensure power stability under extreme misalignment while enabling scalability to 3.3-kW applications, adopts symmetric geometry ($l_p = l_s = 400$ mm, $h = 50$ mm), wire diameters ($d_p = 2.32$ mm, $d_s = 2.53$ mm), and operational

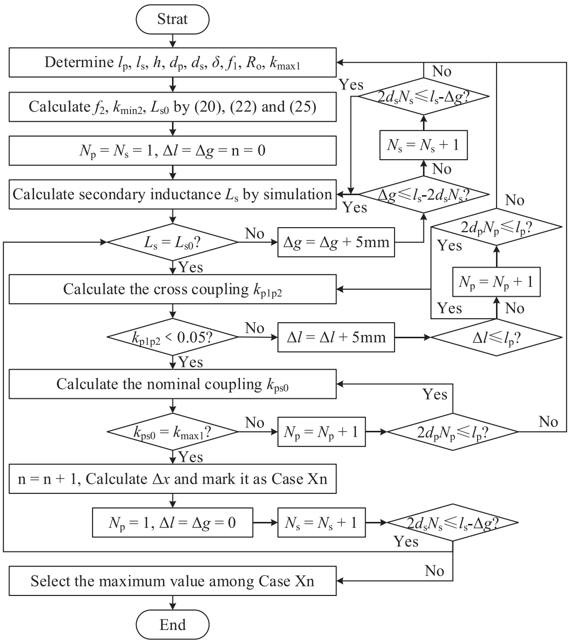

Fig. 6. Flowchart of the magnetic coupler design.

constraints ($f_1 = 85$ kHz, $\delta = 5\%$, $R_o = 15\ \Omega$, $k_{\max 1} = 0.25$). Optimized parameters ($N_p = 8$, $N_s = 6$, $\Delta l = 105$ mm, and $\Delta g = 190$ mm) validate the methodology, achieving $\Delta x = 80\%$ (320 mm lateral tolerance). The coupling coefficient variations (k_{p1s}, k_{p2s}, k_{p1p2}) versus X-, Y-, and Z-axis misalignment are depicted in Fig. 7. The working couplings k_{p1s} and k_{p2s} maintain matched magnitude and polarity across X- and Z-axis displacements, while cross coupling k_{p1p2} remains negligible ($<$0.03). However, Y-axis misalignment disrupts this symmetry, causing opposing trends in k_{p1s} and k_{p2s} due to differential flux linkage variations, as illustrated in Fig. 7(b). This directional selectivity makes the design ideal for applications with constrained Y-axis motion.

1) Rail-guided wireless charging systems, where lateral (X-axis) deviations dominate along track extensions [35].
2) Static EVs charging, where vehicle alignment primarily occurs along the Y-axis via mechanical guidance systems, leaving X-axis positioning uncontrolled [6].
3) IMDs, where Z-axis airgap variations due to anatomical differences require inherent compensation [5].

It should be noted that while this article employs an OLDD-DS coupler optimized for X-axis misalignment tolerance, the reconfiguration methodology itself is coil-agnostic. Any coil pair satisfying $k_{p1s} = k_{p2s}$ and $k_{p1p2} < 0.05$ (e.g., bipolar DD [15], multi-layer solenoids [17] or optimized planar structures [36]) can leverage the proposed dual-frequency switching. The parametric design remains identical; only the coupler's spatial flux distribution requires reoptimization for target misalignment ranges.

C. Frequency Switching Control

Theoretical analysis in Fig. 4 suggests coupling coefficient k_{ps} governs frequency switching criteria. However, practical implementation complexities render k_{ps} estimation unreliable for power-state determination. The proposed method directly estimates load output power P_o to guide frequency transitions. Leveraging $k_{p1s} = k_{p2s}$ (magnitude and polarity equivalence), P_o is calculated via primary-side measurements of inverter output voltage U_{AB} and current I_{p1} using (5) and (12), eliminating secondary-side communication. Fig. 8 illustrates a frequency-mode switching implementation. The system initiates operation at f_1 or f_2, continuously evaluating P_o against thresholds [$P_{o\_\min}$, $P_{o\_\max}$]. Upon P_o exceeds this range, phase-continuous impedance matching at k_{cri} executes frequency switching ($f_1 \leftrightarrow f_2$) within tens of milliseconds, eliminating system shutdown/restart requirements. Persistent out-of-bound P_o postswitching indicates invalid coupling conditions ($k_{ps} < k_{\min 2}$ or $k_{\text{ps}} > k_{\max 1}$), prompting system shutdown. Crucially, this method requires constant load resistance R_o to ensure P_o calculability via U_{AB} and I_{p1} measurements alone.

TABLE I
Parameters of Experimental Prototype

Parameter	Value	Parameter	Value
U_D	300 V	α	0.37
R_o	15 Ω	L_{p1}	118.24 μH
P_{oset}	500 W	L_{p2}	118.22 μH
δ	5%	L_s	165.57 μH
f_1	85 kHz	C_{p1}	18.79 nF
f_2	133.96 kHz	C_{p2}	18.80 nF
β	1.58	L_{eq}	68.22 μH
k_{min2}	0.1006	C_{p0}	34.58 nF
k_{ex2}	0.1263	L_{p0}	40.72 μH
k_{cri}	0.1585	C_s	14.91 nF
k_{ex1}	0.1990	C_{s1}	67.13 nF
k_{max1}	0.2498	L_{s1}	30.11 μH

IV. Experimental Validation

A. Experimental Prototype

To validate the availability of the proposed reconfigurable IPT system, a 500-W experimental prototype was constructed as shown in Fig. 9. Key parameters summarized in Table I, where all capacitance values represent measured parameters achieved through strategic combinations of commercially available components. The dual-frequency operation demonstrates complementary coupling adaptation ranges: at $f_2 = 133.96$ kHz, the effective coupling range spans $k_{ps} \in [0.1006, 0.1585]$; switching to $f_1 = 85$ kHz extends this range to $k_{ps} \in [0.1585, 0.2498]$. The test configuration employs an IT6534D dc source (transmitter side), IT8817B electronic load (receiver side), DLM3034 oscilloscope for waveform capture, and PX8000 power analyzer for precision measurements.

Given the coupled resonance nature of the reconfigurable topology, rigorous tolerance analysis focuses on dominant parameters L_{eq} (for f_1-mode) and C_{p1} (for f_2-mode), with variations bounded at ±3% and ±2% respectively, reflecting practical

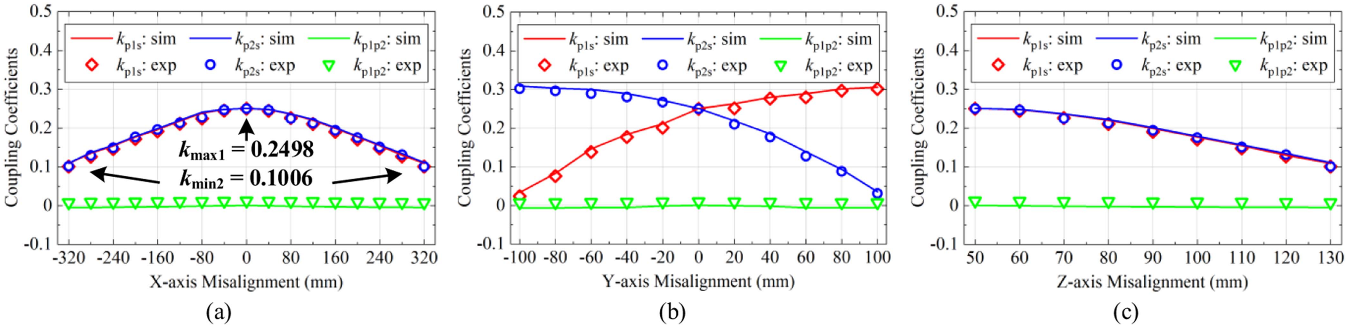

Fig. 7. Simulation and experimental results of coupling coefficients varying with three directional misalignments. (a) *X*-axis. (b) *Y*-axis. (c) *Z*-axis.

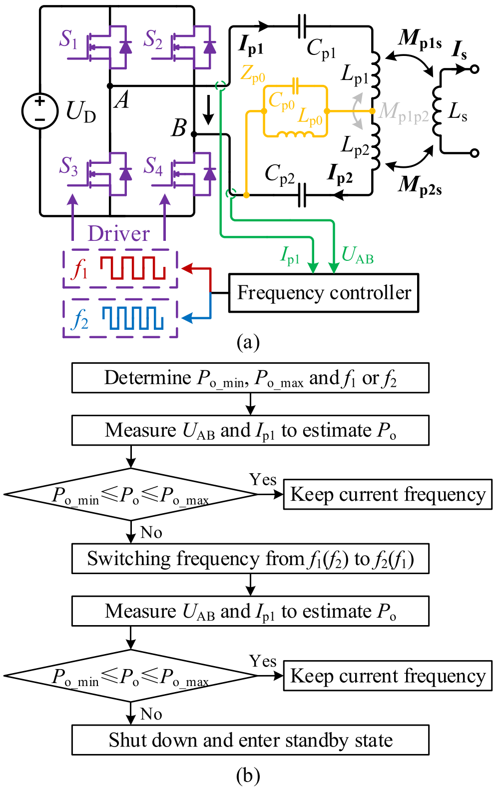

Fig. 8. One implementation of switching between dual-frequency modes. (a) Control diagram of frequency switching. (b) Flowchart of the controller.

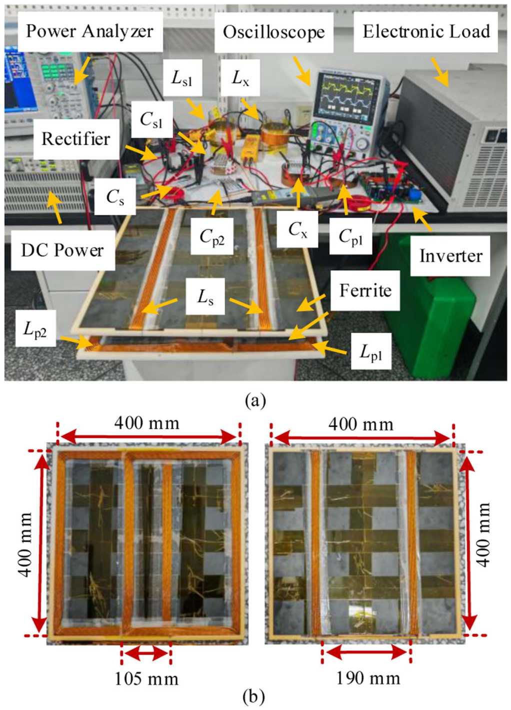

Fig. 9. Experimental prototype. (a) Overall setup. (b) Coil structure.

manufacturing limits. As illustrated in Fig. 10, these deviations induce predictable shifts in power transfer characteristics. Specifically, decreasing L_{eq} from +3% to −3% of nominal and C_{p1} from +2% to −2% translates both the P_{o1}-k_{ps} and P_{o2}-k_{ps} curves leftward and upward due to (9)–(10) and (16)–(17)—reducing k_{ex1} while increasing P_{o1_max}, with analogous f_2-mode effects expanding left-half curve regions. Simultaneously, worst-case tolerance stacking (L_{eq} at +3%, C_{p1} at −2%) reduces critical coupling k_{cri} by 1.58%, consistent with (20) sensitivity analysis. Crucially, under maximum simulated deviations (L_{eq} at −3%, C_{p1} at +2%), the resultant power fluctuation δ increases merely 0.8% (5.0%→5.8%). Experimentally, measurements of the compensation components demonstrate maximum deviations of less than 1% from theoretical calculations. This high degree of component matching ensures the critical parameter alignment required for operational accuracy across both dual-frequency modes.

B. Experimental Results

Fig. 11 presents the variation of the system power fluctuation coefficient δ versus *X*-, *Y*-, and *Z*-axis misalignment, complementing the misalignment tolerance characteristics in Fig. 7. Within the $\delta \leq 5\%$ stability boundary, the system achieves exceptional multiaxis performance: ±320 mm (80% of coil diameter) lateral tolerance along *X*-axis and 50–130 mm (160% of nominal airgap) vertical tolerance along *Z*-axis. Experimental validation confirms constrained *Y*-axis tolerance (±40 mm, 10% of coil diameter), beyond which asymmetric flux linkage disrupts the critical condition $k_{p1s} = k_{p2s}$, resulting in >45% coupling asymmetry [see Fig. 7(b)] and shutdown due to power instability

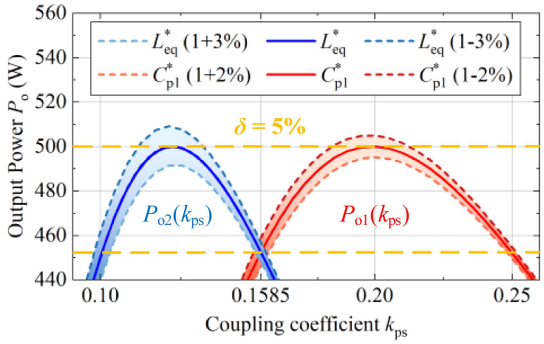

Fig. 10. Tolerance analysis of power transfer stability versus L_{eq} and C_{p1} variations.

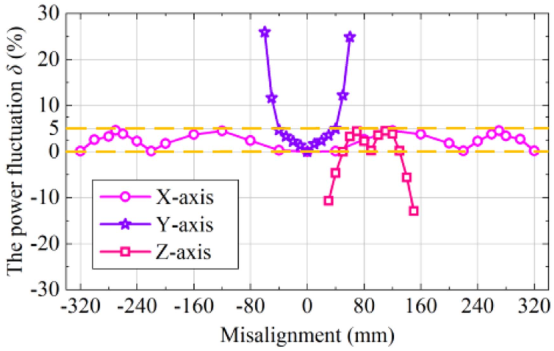

Fig. 11. Power fluctuation coefficient δ versus misalignment.

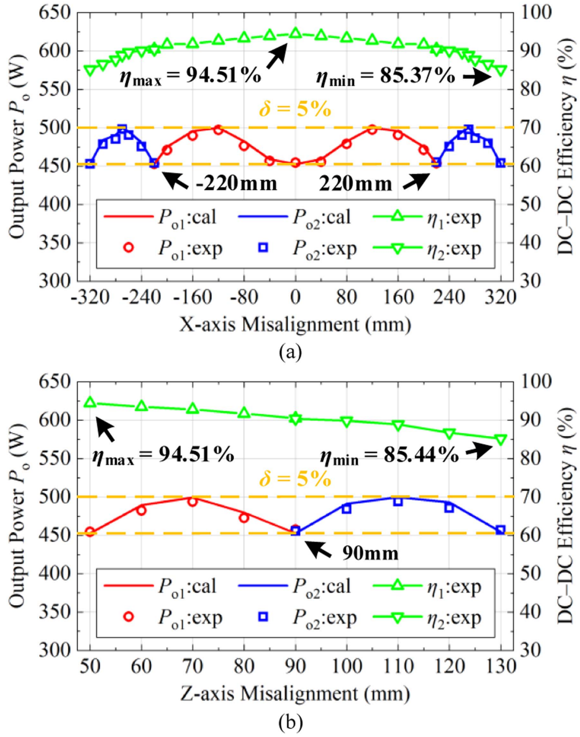

(a)

(b)

Fig. 12. Calculation and experimental results of output power and DC–DC efficiency with misalignments. (a) *X*-axis. (b) *Z*-axis.

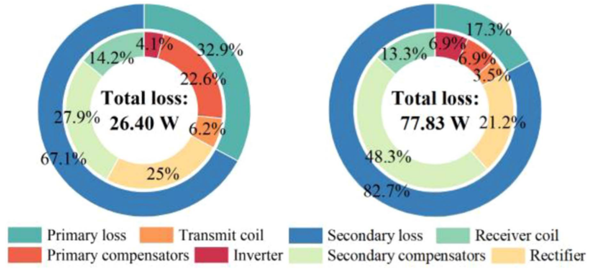

(a)

(b)

Fig. 13. Power loss distributions. (a) f_1, $X = 0$ mm. (b) f_2, $X = 320$ mm.

(>5%). This directional selectivity constitutes a deliberate design tradeoff: while *Y*-axis displacement is inherently restricted in target deployment scenarios, the compromised *Y*-immunity enables record *X/Z*-axis tolerance. The *Y*-constraint thus reflects an optimized system strategy rather than a fundamental limitation.

Fig. 12 demonstrates measured output power and dc–dc efficiency versus *X*-axis displacement and *Z*-axis airgap. Experimental results align closely with theoretical predictions, showing P_o fluctuations between 452.22 W and 498.15 W across $k_{ps} \in [0.1, 0.25]$. Per (18), power variations remain below the 5% design threshold throughout this coupling range. Peak power points occur at critical offsets: $X = 120/270$ mm and $Z = 70/110$ mm. To maintain stable power transfer, frequency switching is triggered at $X = 220$ mm or $Z = 90$ mm, extending operational continuity beyond single-frequency limitations. System efficiency exceeds 85% across all tested conditions, peaking at 94.51% in aligned configuration ($X = 0$, $Y = 0$, and $Z = 50$ mm). Fig. 13 details loss distributions at efficiency extrema ($X = 0$ and $X = 320$ mm) further validate the design's robustness against misalignment-induced parasitic effects. Notably, the proposed method achieves smooth power/efficiency transitions at critical coupling k_{cri} without oscillations or abrupt jumps, outperforming methods in [28], [29], [30], [31], and [34] where transient spikes were reported.

Fig. 14 characterizes system output power variation across load resistances, where measurements for $R_o = \{8, 15, 25\}$ Ω reveal consistent rightward translation of the *P*–*k* curve under increasing R_o, while maintaining invariant peak power (500 W) and coupling ratio ($k_{\max}/k_{\min} = 250\%$). This confirms that although load resistance variation shifts the k_{ps} operating points for given output powers, it preserves both power extrema and the fundamental coupling range ratio. For IPT systems requiring operation within specified k_{ps} bounds (e.g., 0.1–0.25), however, active stabilization of R_{o} becomes imperative to maintain consistent power transfer characteristics across the designated coupling range.

Fig. 15 illustrates input impedance Z_{in} and phase angle θ_{in} versus k_{ps} calculated from Table I parameters via (23). As k_{ps} increases from 0.1006 to 0.1585 (133.96 kHz), Z_{in} ascends from 86.15 Ω to 135.77 Ω while θ_{in} descends from 57.60° to 32.40°. Conversely, when k_{ps} extends from 0.1585 to 0.2498 (85 kHz), Z_{in} decreases symmetrically back to 86.15 Ω with θ_{in} rising to 57.60°. This bidirectional impedance-phase relationship ensures seamless overlap at $k_{\text{cri}} = 0.1585$, fundamentally

TABLE II
COMPARISON WITH OTHER METHODS REPORTED IN PREVIOUS LITERATURES

Ref.	System frequency	Coupling variation	Misalignment tolerance (Misalignment percentage)	Output fluctuation	Output characteristic	Maximum power	Efficiency
Feng et al. [23]	200 kHz	0.08–0.2 (250%)	x-misalignment: ±40 mm (41.7%) y-misalignment: ±40 mm (41.7%) z-misalignment: 25 mm-45 mm (80%)	11.1%	Constant power	70 W	66%–73%
Feng et al. [25]	200 kHz	0.14–0.28 (200%)	N/A	11.1%	Constant power	100 W	83.5%–87.5%
Yang et al. [34]	236 kHz 257 kHz	0.115–0.27 (235%)	x-misalignment: ±150 mm (50%) y-misalignment: ±150 mm (50%) z-misalignment: 80 mm-160 mm (100%)	5.6%	Constant power	750 W	91.46%–95.52%
Qu et al. [37]	85 kHz	0.1–0.2 (200%)	x-misalignment: ±200 mm (50%) y-misalignment: N/A z-misalignment: 130 mm-190 mm (46.2%)	5%	Constant voltage	3.5 kW	87%–93%
Zhao et al. [38]	200 kHz	0.12–0.245 (204%)	x-misalignment: N/A y-misalignment: ±100 mm (50%) z-misalignment: N/A	11.1%	Constant power	400 W	87%–92%
Chen et al. [39]	90 kHz	0.14–0.29 (207%)	x-misalignment: ±180 mm (40%) y-misalignment: ±180 mm (40%) z-misalignment: N/A	5%	Constant current	3.4 kW	92.1%–92.3%
Mai et al. [40]	85 kHz	0.1–0.25 (250%)	x-misalignment: ±225 mm (50%) y-misalignment: -30 mm-+50 mm (11.1%) z-misalignment: 130 mm-220 mm (69.2%)	5%	Constant current	3.4 kW	92%–96%
Chen et al. [41]	250 kHz	0.1–0.4 (400%)	N/A	17.5%	Constant power	400 W	87.5%–95.6%
This article	**85 kHz 133.96 kHz**	**0.1–0.25 (250%)**	**x-misalignment: ±320 mm (80%) y-misalignment: ±40 mm (10%) z-misalignment: 50 mm-130 mm (160%)**	**5%**	**Constant power**	**500W**	**85.37%-94.51%**

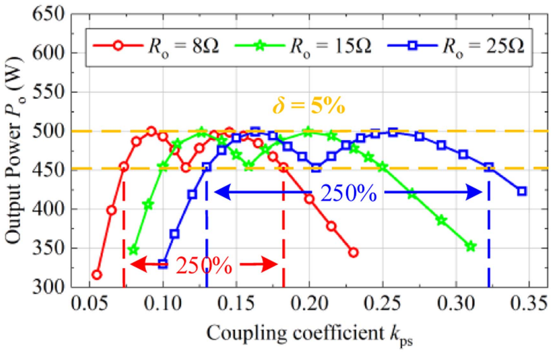

Fig. 14. Measured *P*-*k* curves with different loads.

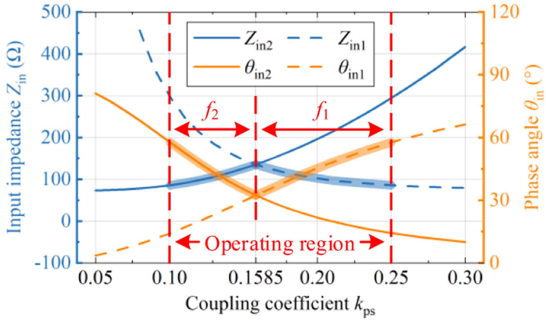

Fig. 15. Input impedance and its phase angle of the reconfigurable topology.

enabling smooth power/efficiency transitions during frequency switching. Crucially, the inductive nature of Z_{in} guarantees ZVS across all operational states. Experimental waveforms in Fig. 16 confirm sustained ZVS achievement.

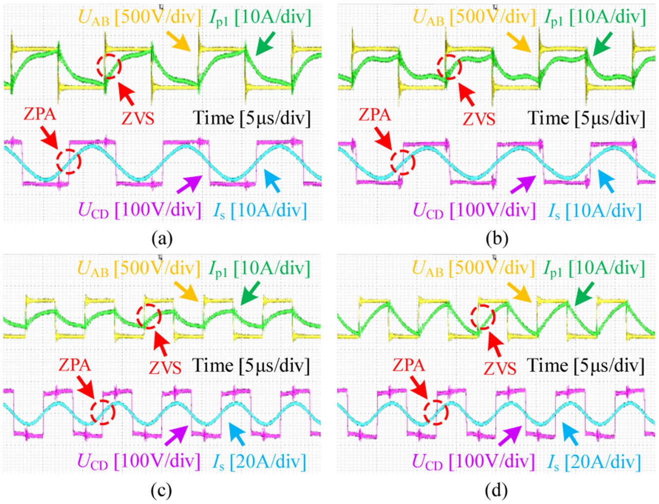

(a) (b)

(c) (d)

Fig. 16. Experimental waveforms. (a) f_1, $X = 0$. (b) f_1, $X = 220$ mm. (c) f_2, $X = 220$ mm. (d) f_2, $X = 320$ mm.

C. Comparison and Discussion

The proposed reconfigurable IPT system demonstrates superior performance through comprehensive comparison with existing methods, as quantitatively validated in Table II. Compared with methods [25], [34], [38], the proposed method achieves smaller output fluctuation within a wider range of coupling variation. In contrast to methods [37], [39], the proposed method exhibits a larger permissible coupling variation while maintaining identical output fluctuation. When benchmarked against method [23], the proposed method reduces output fluctuations by over 50% under the same coupling variation conditions. In comparison with methods [40], the proposed method shows significantly superior lateral (*X*-axis) and vertical (*Z*-axis) misalignment tolerance ranges, despite achieving comparable coupling variation and output fluctuation performance. Relative to method [41], although the coupling variation is lower by 150%, the output fluctuation is suppressed to 28.6% of its value, establishing an optimal performance trade-off.

Admittedly, it should be noted that the proposed system incorporates a detuned topology in one of its compensation networks. This configuration shares similarities with methodologies documented in [23], [24], [25], [28], [29], [30], [31], [34], and [41], potentially resulting in elevated reactive power levels. Furthermore, due to the displacement constraint of the designed magnetic coupler along the *Y*-axis, the proposed methodology demonstrates higher applicability in low-to-mid power applications (0.05–3.3 kW) where significant misalignment may occur in one spatial dimension (*X*- or *Z*-axis) while maintaining minimal displacement in the orthogonal direction (*Y*-axis), particularly in scenarios requiring critical performance metrics such as output efficiency and power stability. Typical implementation scenarios include IMDs [5], lighting systems [42], and kitchen appliances [43].

V. CONCLUSION

This article proposes a dual discrete-frequency reconfigurable IPT system to achieve stable power transfer across extended coupling variation. By exploiting parallel resonant characteristics, the compensation network is dynamically reconfigured between dual-coupled SP-S and detuned S-S topologies at two discrete frequencies, both exhibiting flat *P*–*k* segments. A simple non-iterative parameter design method directly determines operating frequencies to achieve full-range continuous power coverage, eliminating frequency search procedures. The transmitter employs an OLDD coil coupled to a DS receiver, enhancing misalignment tolerance. Experimental results validate that the proposed system maintains merely 5% power fluctuation with 85.37%–94.51% efficiency across 250% coupling variation (corresponding to ±320 mm *X*-axis misalignment or 50–130 mm *Z*-axis airgap variation), demonstrating superior misalignment tolerance. Crucially, the complementary impedance characteristics between topologies enable smooth power/efficiency transitions during frequency switching. The methodology proves particularly suitable for low-to-mid power applications requiring substantial unidirectional misalignment tolerance. Future work will focus on magnetic couplers with multidimensional misalignment adaptability.

REFERENCES

[1] Z. Zhang, H. Pang, A. Georgiadis, and C. Cecati, “Wireless power transfer—An overview,” *IEEE Trans. Ind. Electron.*, vol. 66, no. 2, pp. 1044–1058, Feb. 2019.

[2] Y. Lan et al., “Research on impedance boundary and tolerance zone for improving wireless charging interoperability evaluation of electric vehicles,” *IEEE Trans. Power Electron.*, vol. 39, no. 10, pp. 12035–12040, Oct. 2024.

[3] C. Zhang et al., “A strong misalignment-tolerance wireless power transfer system based on dynamic diffusion magnetic field for unmanned aerial vehicle applications,” *IEEE Trans. Power Electron.*, vol. 39, no. 11, pp. 14129–14134, Nov. 2024.

[4] Z. Yan et al., “Frequency optimization of a loosely coupled underwater wireless power transfer system considering eddy current loss,” *IEEE Trans. Ind. Electron.*, vol. 66, no. 5, pp. 3468–3476, May 2019.

[5] C. Liu, C. Jiang, J. Song, and K. T. Chau, “An effective sandwiched wireless power transfer system for charging implantable cardiac pacemaker,” *IEEE Trans. Ind. Electron.*, vol. 66, no. 5, pp. 4108–4117, May 2019.

[6] K. Song et al., “Design of DD coil with high misalignment tolerance and low EMF emissions for wireless electric vehicle charging systems,” *IEEE Trans. Power Electron.*, vol. 35, no. 9, pp. 9034–9045, Sep. 2020.

[7] C. Xia, W. Wang, S. Ren, X. Wu, and Y. Sun, “Robust control for inductively coupled power transfer systems with coil misalignment,” *IEEE Trans. Power Electron.*, vol. 33, no. 9, pp. 8110–8122, Sep. 2018.

[8] Z. Huang, S.-C. Wong, and C. K. Tse, “Control design for optimizing efficiency in inductive power transfer systems,” *IEEE Trans. Power Electron.*, vol. 33, no. 5, pp. 4523–4534, May 2018.

[9] S. Chen, H. Li, and Y. Tang, “Extending the operating region of inductive power transfer systems through dual-side cooperative control,” *IEEE Trans. Ind. Electron.*, vol. 67, no. 11, pp. 9302–9312, Nov. 2020.

[10] Z. Zhang, S. Shen, Z. Liang, S. H. K. Eder, and R. Kennel, “Dynamic-balancing robust current control for wireless drone-in-flight charging,” *IEEE Trans. Power Electron.*, vol. 37, no. 3, pp. 3626–3635, Mar. 2022.

[11] E. Gati, G. Kampitsis, and S. Manias, “Variable frequency controller for inductive power transfer in dynamic conditions,” *IEEE Trans. Power Electron.*, vol. 32, no. 2, pp. 1684–1696, Feb. 2017.

[12] Z. Zhang, F. Zhu, D. Xu, P. T. Krein, and H. Ma, “An integrated inductive power transfer system design with a variable inductor for misalignment tolerance and battery charging applications,” *IEEE Trans. Power Electron.*, vol. 35, no. 11, pp. 11544–11556, Nov. 2020.

[13] U. D. Kavimandan, S. M. Mahajan, and C. W. Van Neste, “Analysis and demonstration of a dynamic ZVS angle control using a tuning capacitor in a wireless power transfer system,” *IEEE J. Emerg. Sel. Topics Power Electron.*, vol. 9, no. 2, pp. 1876–1890, Apr. 2021.

[14] M. Budhia, J. T. Boys, G. A. Covic, and C.-Y. Huang, “Development of a single-sided flux magnetic coupler for electric vehicle IPT charging systems,” *IEEE Trans. Ind. Electron.*, vol. 60, no. 1, pp. 318–328, Jan. 2013.

[15] A. Zaheer, H. Hao, G. A. Covic, and D. Kacprzak, “Investigation of multiple decoupled coil primary pad topologies in lumped IPT systems for interoperable electric vehicle charging,” *IEEE Trans. Power Electron.*, vol. 30, no. 4, pp. 1937–1955, Apr. 2015.

[16] S. Kim, G. A. Covic, and J. T. Boys, “Tripolar pad for inductive power transfer systems for EV charging,” *IEEE Trans. Power Electron.*, vol. 32, no. 7, pp. 5045–5057, Jul. 2017.

[17] J. Mai, Y. Wang, Y. Yao, M. Sun, and D. Xu, “High-misalignment-tolerant IPT systems with solenoid and double D pads,” *IEEE Trans. Ind. Electron.*, vol. 69, no. 4, pp. 3527–3535, Apr. 2022.

[18] C. Chen, C. Q. Jiang, X. Wang, L. Mo, W. Guo, and S. Ren, “Terrace-shaped core design method for inductive power transfer system considering uniform magnetic flux distribution,” *IEEE Trans. Ind. Electron.*, vol. 72, no. 8, pp. 7795–7806, Aug. 2025, doi: 10.1109/TIE.2025.3528499.

[19] L. Zhao, D. J. Thrimawithana, and U. K. Madawala, “Hybrid bidirectional wireless EV charging system tolerant to pad misalignment,” *IEEE Trans. Ind. Electron.*, vol. 64, no. 9, pp. 7079–7086, Sep. 2017.

[20] L. Zhao, D. J. Thrimawithana, U. K. Madawala, A. P. Hu, and C. C. Mi, “A misalignment-tolerant series-hybrid wireless EV charging system with integrated magnetics,” *IEEE Trans. Power Electron.*, vol. 34, no. 2, pp. 1276–1285, Feb. 2019.

[21] Y. Chen, B. Yang, Z. Kou, Z. He, G. Cao, and R. Mai, “Hybrid and reconfigurable IPT systems with high-misalignment tolerance for constant current and constant voltage battery charging,” *IEEE Trans. Power Electron.*, vol. 33, no. 10, pp. 8259–8269, Oct. 2018.

[22] Y. Chen et al., “A hybrid inductive power transfer system with misalignment tolerance using quadruple-d quadrature pads,” *IEEE Trans. Power Electron.*, vol. 35, no. 6, pp. 6039–6049, Jun. 2020.

[23] H. Feng, T. Cai, S. Duan, X. Zhang, H. Hu, and J. Niu, “A dual-side-detuned series–series compensated resonant converter for wide charging region in a wireless power transfer system,” *IEEE Trans. Ind. Electron.*, vol. 65, no. 3, pp. 2177–2188, Mar. 2018.

[24] H. Feng, T. Cai, S. Duan, J. Zhao, X. Zhang, and C. Chen, “An LCC-compensated resonant converter optimized for robust reaction to large coupling variation in dynamic wireless power transfer,” *IEEE Trans. Ind. Electron.*, vol. 63, no. 10, pp. 6591–6601, Oct. 2016.

[25] H. Feng, A. Dayerizadeh, and S. M. Lukic, “A coupling-insensitive X-type IPT system for high position tolerance,” *IEEE Trans. Ind. Electron.*, vol. 68, no. 8, pp. 6917–6926, Aug. 2021.

[26] Z. Yan et al., “Fault-tolerant wireless power transfer system with a dual-coupled LCC-S topology,” *IEEE Trans. Veh. Technol.*, vol. 68, no. 12, pp. 11838–11846, Dec. 2019.

[27] F. Lu, H. Zhang, H. Hofmann, W. Su, and C. C. Mi, “A dual-coupled LCC-compensated IPT system with a compact magnetic coupler,” *IEEE Trans. Power Electron.*, vol. 33, no. 7, pp. 6391–6402, Jul. 2018.

[28] Y. Chen et al., “Reconfigurable topology for IPT system maintaining stable transmission power over large coupling variation,” *IEEE Trans. Power Electron.*, vol. 35, no. 5, pp. 4915–4924, May 2020.

[29] Y. Zhang et al., “Misalignment-tolerant dual-transmitter electric vehicle wireless charging system with reconfigurable topologies,” *IEEE Trans. Power Electron.*, vol. 37, no. 8, pp. 8816–8819, Aug. 2022.

[30] P. Zhao, J. Liang, H. Wang, and M. Fu, “Detuned LCC/S-S compensation for stable-output inductive power transfer system under ultrawide coupling variation,” *IEEE Trans. Power Electron.*, vol. 38, no. 10, pp. 12342–12347, Oct. 2023.

[31] C. Chen, C. Q. Jiang, T. Ma, X. Wang, Y. Fan, and J. Xiang, “Misalignment Tolerance Extension for Inductive Power Transfer System by Utilizing Slight Frequency-Detuned Compensation,” *IEEE Trans. Transp. Electrific.*, vol. 10, no. 4, pp. 9748–9760, Dec. 2024.

[32] Z. Huang, S.-C. Wong, and C. K. Tse, “Design of a single-stage inductive-power-transfer converter for efficient EV battery charging,” *IEEE Trans. Veh. Technol.*, vol. 66, no. 7, pp. 5808–5821, Jul. 2017.

[33] L. Yang, X. Li, S. Liu, Z. Xu, and C. Cai, “Analysis and design of an LCCC/S-compensated WPT system with constant output characteristics for battery charging applications,” *IEEE J. Emerg. Sel. Topics Power Electron.*, vol. 9, no. 1, pp. 1169–1180, Feb. 2021.

[34] B. Yang et al., “A detuned S-S compensated IPT system with two discrete frequencies for maintaining stable power transfer versus wide coupling variation,” *IEEE Trans. Transp. Electrific.*, vol. 9, no. 3, pp. 3836–3848, Sep. 2023.

[35] Y. Jiang, K. Chen, Z. Zhao, L. Yuan, T. Tan, and Q. Lin, “Designing an M-Shape Magnetic Coupler for the Wireless Charging System in Railway Applications,” *IEEE Trans. Power Electron.*, vol. 37, no. 1, pp. 1059–1073, Jan. 2022.

[36] D. Bui, Q. Zhu, L. Zhao, and A. P. Hu, “Concentric-coil hybrid IPT system with improved tolerance to coupling and load variations,” *IEEE J. Emerg. Sel. Topics Power Electron.*, vol. 10, no. 4, pp. 4913–4922, Aug. 2022.

[37] X. Qu, Y. Yao, D. Wang, S. Wong, and C. K. Tse, “A family of hybrid IPT topologies with near load-independent output and high tolerance to pad misalignment,” *IEEE Trans. Power Electron.*, vol. 35, no. 7, pp. 6867–6877, Jul. 2020.

[38] J. Zhao, T. Cai, S. Duan, H. Feng, C. Chen, and X. Zhang, “A general design method of primary compensation network for dynamic WPT system maintaining stable transmission power,” *IEEE Trans. Power Electron.*, vol. 31, no. 12, pp. 8343–8358, Dec. 2016.

[39] Y. Chen, R. Mai, Y. Zhang, M. Li, and Z. He, “Improving misalignment tolerance for IPT system using a third-coil,” *IEEE Trans. Power Electron.*, vol. 34, no. 4, pp. 3009–3013, Apr. 2019.

[40] R. Mai, B. Yang, Y. Chen, N. Yang, Z. He, and S. Gao, “A misalignment tolerant IPT system with intermediate coils for constant-current output,” *IEEE Trans. Power Electron.*, vol. 34, no. 8, pp. 7151–7155, Aug. 2019.

[41] Y. Chen, S. He, B. Yang, S. Chen, Z. He, and R. Mai, “Reconfigurable rectifier-based detuned series-series compensated IPT system for anti-misalignment and efficiency improvement,” *IEEE Trans. Power Electron.*, vol. 38, no. 2, pp. 2720–2729, Feb. 2023.

[42] W. Liu, K. T. Chau, C. H. T. Lee, C. Jiang, W. Han, and W. H. Lam, “A wireless dimmable lighting system using variable-power variable-frequency control,” *IEEE Trans. Ind. Electron.*, vol. 67, no. 10, pp. 8392–8404, Oct. 2020.

[43] M. Itraj and W. Ettes, “Topology study for an inductive power transmitter for cordless kitchen appliances,” in *Proc. IEEE PELS Workshop Emerg. Technol., Wireless Power Transf.*, 2018, pp. 1–8.